

Multimode interference effect and self-imaging principle in two-dimensional silicon photonic crystal waveguides for terahertz waves

Yao Zhang, Zhangjian Li, and Baojun Li

State Key Laboratory of Optoelectronic Materials and Technologies, Institute of Optoelectronic and Functional Composite Materials, Sun Yat-Sen University, Guangzhou 510275, China
stslbj@mail.sysu.edu.cn

Abstract: Applicability of multimode interference effect and self-imaging principle for terahertz waves in two-dimensional silicon photonic crystal waveguides are investigated by modeling and computation. The results show that the multimode interference effect and the self-imaging principle are applicable for terahertz waves. As an example, a splitter and a filter for terahertz waves have been proposed, calculated and analyzed by finite-difference time-domain method based on the multimode interference effect and the self-imaging principle.

©2006 Optical Society of America

OCIS codes: (130.3120) Integrated optics devices; (130.2790) Guided waves

References and links

1. R. Köhler, A. Tredicucci, F. Beltram, H. E. Beere, E. H. Linfield, A. G. Davies, D. A. Ritchie, R. C. Iotti and F. Rossi, "Terahertz semiconductor-heterostructure laser," *Nature* **417**, 156-159 (2002).
2. G. L. Carr, M. C. Martin, W. R. McKinney, K. Jordan, G. R. Neil and G. P. Williams, "High-power terahertz radiation from relativistic electrons," *Nature* **420**, 153-156 (2002).
3. A. Borak, "Toward bridging the terahertz gap with silicon-based lasers," *Science* **308**, 638-639 (2005).
4. O. Astafiev, S. Komiyama and T. Kutsuwa, "Double quantum dots as a high sensitive submillimeter-wave detector," *Appl. Phys. Lett.* **79**, 1199-1201 (2001).
5. D. Clery, "Terahertz on a chip," *Science* **297**, 763 (2002).
6. N. C. J. van der Valk and P. C. M. Planken, "Electro-optic detection of subwavelength terahertz spot sizes in the near field of a metal tip," *Appl. Phys. Lett.* **81**, 1558-1560 (2002).
7. T. A. Liu, M. Tani, M. Nakajima, M. Hangyo and C. L. Pan "Ultrabroadband terahertz field detection by photoconductive antennas based on multi-energy arsenic-ion-implanted GaAs and semi-insulating GaAs," *Appl. Phys. Lett.* **83**, 1322-1324 (2003).
8. K. Wang and D. M. Mittleman, "Metal wires for terahertz wave guiding," *Nature* **432**, 376-379, (2004).
9. D. Dragoman and M. Dragoman, "Terahertz fields and applications," *Prog. Quantum Electron.* **28**, 1-66, (2004).
10. H. Kitahara, N. Tsumura, H. Kondo, M. W. Takeda, J. W. Haus, Z. Yuan, N. Kawai, K. Sokada and K. Inoue, "Terahertz wave dispersion in two-dimensional photonic crystals," *Phys. Rev. B* **64**, 045202 (2001).
11. H. Han, H. Park, M. Cho, and J. Kim, "Terahertz pulse propagation in a plastic photonic crystal fiber," *Appl. Phys. Lett.* **80**, 2634-2636 (2002).
12. C. Jin, B. Cheng, Z. Li, D. Zhang, L. M. Li and Z. Q. Zhang, "Two dimensional metallic photonic crystal in the THz range" *Opt. Commun.* **166**, 9-13 (1999).
13. N. Jukam and M. S. Sherwin, "Two-dimensional terahertz photonic crystals fabricated by deep reactive ion etching in Si," *Appl. Phys. Lett.* **83**, 21-23 (2003).
14. C. Lin, C. Chen, G. J. Schneider, P. Yao, S. Shi, A. Sharkawy and D. W. Prather, "Wavelength scale terahertz two-dimensional photonic crystal waveguides," *Opt. Express* **12**, 5723-5728 (2004), <http://www.opticsexpress.org/abstract.cfm?URI=OPEX-12-23-57231>
15. K. Takagi, K. Seno and A. Kawasaki, "Fabrication of a three-dimensional terahertz photonic crystal using monosized spherical particles," *Appl. Phys. Lett.* **85**, 3681-3683 (2004).
16. T. D. Drysdale, I. S. Gregory, C. Baker, E. H. Linfield, W. R. Tribe and D. R. S. Cumming, "Transmittance of a tunable filter at terahertz frequencies," *Appl. Phys. Lett.* **85**, 5173-5175 (2004).
17. H. Němec, L. Duvillaret, F. Garet, P. Kužel, P. Xavier, J. Richard and D. Raully, "Thermally tunable filter for terahertz range based on a one-dimensional photonic crystal with a defect," *J. Appl. Phys.* **96**, 4072-4075 (2004).

18. H. Kurt and D. S. Citrin, "Photonic crystals for biochemical sensing in the terahertz region," *Appl. Phys. Lett.* **87**, 041108 (2005).
19. A. Bingham, Y. Zhao and D. Grischkowsky, "THz parallel plate photonic waveguides," *Appl. Phys. Lett.* **87**, 051101 (2005).
20. H. J. Kim, I. Park, B. H. O, S. G. Park, E. H. Lee and S. G. Lee, "Self-imaging phenomena in multi-mode photonic crystal line-defect waveguides: application to wavelength de-multiplexing," *Opt. Express* **12**, 5625-5633 (2004),
<http://www.opticsexpress.org/abstract.cfm?URI=OPEX-12-23-5625>
21. L. B. Soldano and E. C. M. Pennings, "Optical multi-mode interference devices based on self-imaging: principles and applications," *J. Lightwave Technol.* **13**, 615-627 (1995).
22. M. Qiu, "Effective index method for heterostructure-slab-waveguide-based two-dimensional photonic crystals," *Appl. Phys. Lett.* **81**, 1163-1165 (2002).
23. S. G. Johnson and J. D. Joannopoulos, "Block-iterative frequency-domain methods for Maxwell's equations in a planewave basis," *Opt. Express* **8**, 173-190 (2001),
<http://www.opticsexpress.org/abstract.cfm?URI=OPEX-8-3-173>

1. Introduction

Due to lack of exploration, there was a terahertz (THz) frequency region called "terahertz gap" in the electromagnetic spectrum. The so-called "terahertz gap" is from 30 μm to 1 mm in wavelength, which is between far-infrared (photonics) and millimeter wave (electronics). Recently, with a progress on THz wave generation [1-3] and detection [4-7], applications of THz waves have been dramatically developed. Accordingly, THz devices operating on photonic principles are becoming more and more attractive, especially since THz wave guiding was achieved in metal wires [8]. Usually, THz wave propagation in natural dielectric materials has a drawback that majority of dielectric materials have large absorption coefficients in the THz region (as a notable exception, silicon is transparent to waves below 10 THz [9]). So current waveguide devices for THz waves tend to be fabricated with artificial materials like photonic crystals (PCs). PCs with predetermined photonic band gaps can provide strong confinement and flexible control for THz waves as they do for light waves. Besides, physical dimensions of THz PCs are in a larger scale than those of PCs for light waves with much shorter wavelengths. These lead to a great convenience in fabrication of PC-based THz waveguide devices. Therefore, research work on PC devices for THz waves has become a hot pursuit very recently and a variety of outcomes can be found in characteristic demonstration [10-12], fabrication [13-15] and application [16-19].

Reported works on PC based THz devices have applied manifold lightwave behaviors. But it is not clear whether the distinct theories and technologies in photonics and electronics can directly be employed in THz region or not. To our knowledge, few of these works have been involved and studied THz waves in multimode interference (MMI) effect and self-imaging principle, which have already been proved to hold true in near infrared multimode PC waveguides [20]. Devices based on the MMI effect are of excellent properties and ease of fabrication. They have also fulfilled many requirements of applications in photonic integrated circuits (PICs) and telecommunication networks [21]. Therefore it is greatly expected that devices based on MMI effect be used in the THz region and open new opportunities for THz waves guiding, routing, dividing, coupling, and multiplexing, etc.

As mentioned above, silicon (Si) is transparent to waves below 10 THz. It also has a refractive index of nearly a constant in the THz region. In addition, in the THz region, scales of structures in Si-based waveguide devices are close to those in large-scale integrated circuits, which can be easily fabricated with current micro-machining and CMOS techniques. These make Si a fairly good material for THz PC based waveguide devices. Therefore, in this paper, we present a study on the MMI effect and the self-imaging principle in two-dimensional (2D) multimode Si PC waveguides for THz waves. With numerical computation and simulation by finite-difference time-domain (FDTD) method, continuous THz wave propagation and field distribution in the multimode PC waveguides are achieved to show a good agreement with the results derived from the self-imaging principles. At last, two device examples are

demonstrated as applications of the work to THz wave filtering and splitting.

2. Models for PCs and multimode PC waveguides

Figure 1 shows two typical 2D PC models: (a) air hole arrays with a triangular lattice in Si (model-I) and (b) Si pillar arrays with a rectangular lattice in air (model-II). To get wide band gaps in the Si PCs so as to guide THz waves in a broad bandwidth, appropriate fill factors related to the ratio of r/a are needed, where a is the lattice constant of the PCs, r is the radius of the air hole in model-I [Fig. 1(a)] or Si pillar in model-II [Fig. 1(b)]. Studies have shown that large band gaps can exist in the two typical PCs when r/a is set to be 0.4 for model-I and 0.18 for model-II. Another factor affecting the PC band gaps is the refractive index of Si. For the THz region with a wavelength region from 30 μm to 1 mm, Si has an index of 3.42. Therefore, an effective index for model-I can be calculated according to method in reference [22]. In our case, the thickness of the Si slab is around 30 μm and so the calculated effective index is 2.95 for the 2D PCs of model-I, which is formed by the Si slab with air holes.

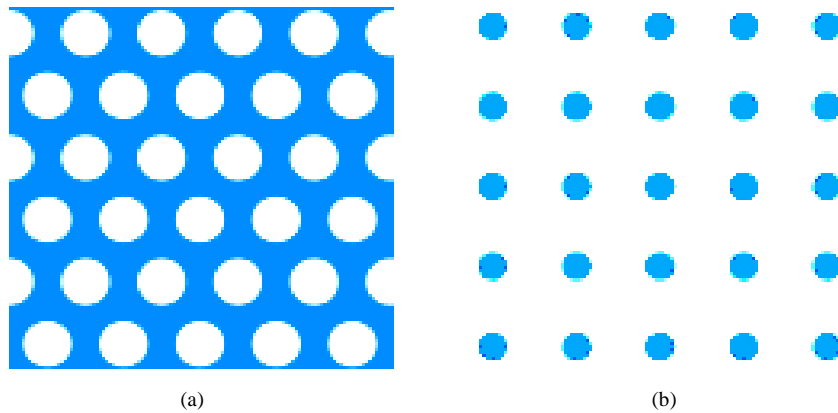
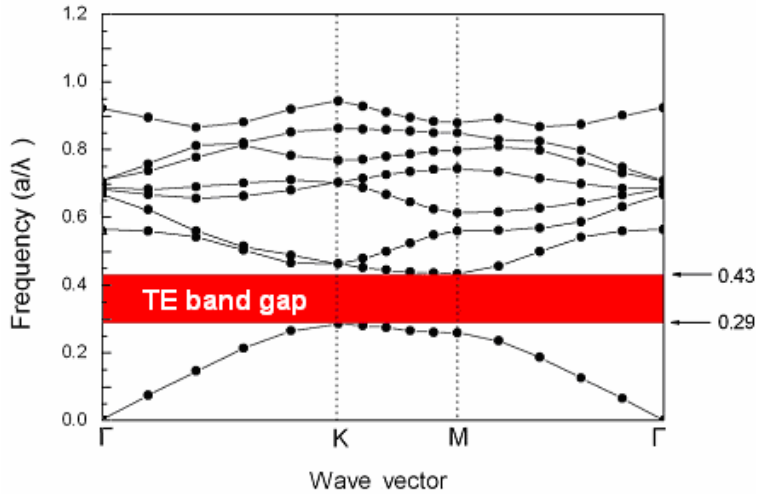
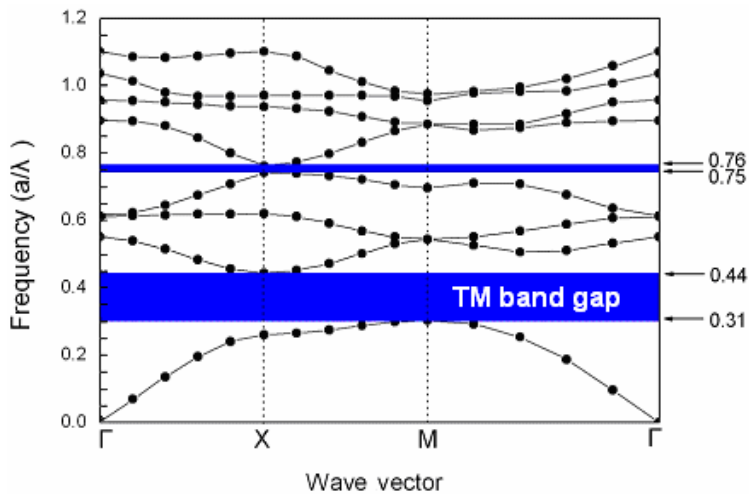


Fig. 1. Typical 2D PC models: (a) air hole array with a triangular lattice in Si (model-I) and, (b) Si pillar array with a rectangular lattice in air (model-II).

Figure 2 shows the band gaps of the two models obtained by using plane wave expansion (PWE) method [23]. It can be seen from Fig. 2 that for the two PC models, a relatively large band gap exists in the frequency ranges of $0.29-0.43(a/\lambda)$ with TE polarization and $0.31-0.44(a/\lambda)$ with TM polarization for model-I and model-II, respectively, where a is the lattice constant of the PC and λ is the wavelength. It should be pointed out that although another small band gap exists for model-II, it is too narrow to be used and so we just consider the larger ones. Considering potential applications in medical and biological fields, THz frequencies are set to be 1.4-2.1 THz, which are informative for absorption in majority large biomolecules [18]. Therefore an appropriate lattice constant of 62 μm is determined for the two models. Accordingly, the radiuses for air holes in model-I and Si pillars in model-II are determined, with values of 25 μm and 11 μm , respectively.



(a)



(b)

Fig. 2. Band gap diagrams for the two models: (a) for model-I, (b) for model-II.

To investigate the applicability of the MMI effect and the self-imaging principle for THz waves in the 2D Si PC models, two MMI structures are proposed as shown in Fig. 3. In Fig. 3, input waveguides are line-defect waveguides formed by removing one row of air holes [Fig. 3(a)] or Si pillars [Fig. 3(b)]. The multimode regions are area defects formed by removing five consecutive rows.

To confirm the number of guided modes supported by the input waveguides and by the multimode regions, dispersion curves for the two structures are calculated by PWE method. The results are shown in Fig. 4. In Fig. 4, the insets are the super-cells used for calculation. From Fig. 4 we can see that for the two models, the input waveguides hold one mode at frequencies of $0.343(a/\lambda)$ and $0.378(a/\lambda)$ and therefore ensure single-mode propagation. The multimode region of model-III holds three modes at $0.343(a/\lambda)$ and two modes at $0.378(a/\lambda)$, respectively, as shown in Fig. 4(a). And, for model-IV, it holds three modes at $0.343(a/\lambda)$ and four modes at $0.378(a/\lambda)$, respectively, as shown in Fig. 4(b).

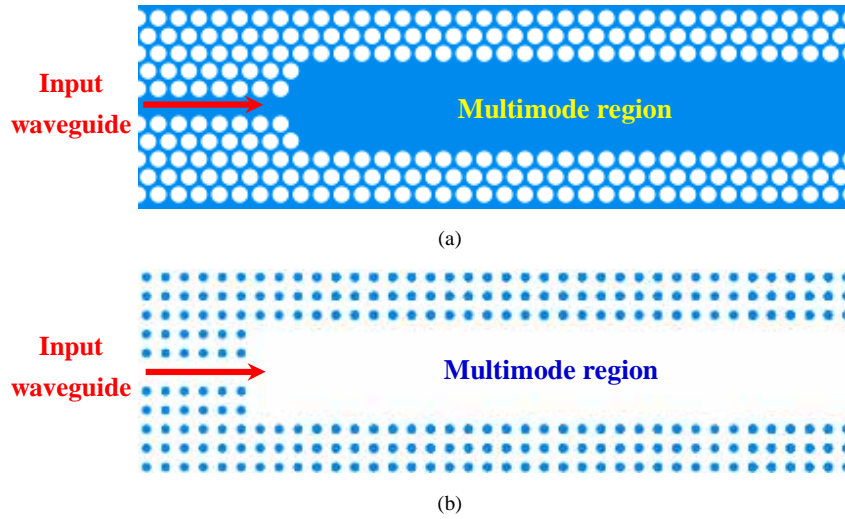


Fig. 3. Models of the proposed MMI structures with line-defect input waveguides and area-defect multimode regions: (a) model-III with a thickness of $37\ \mu\text{m}$, and (b) model-IV with a thickness of $100\ \mu\text{m}$.

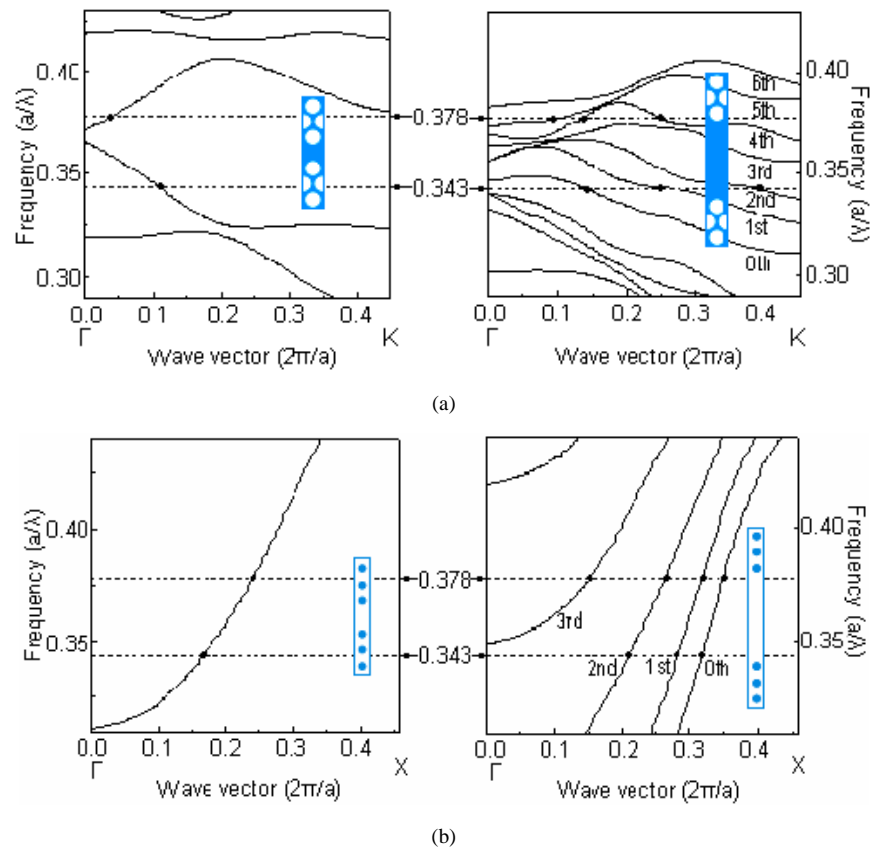


Fig. 4. Dispersion curves for the two structure models in Fig. 3. Input waveguides ensure single-mode propagations at frequencies of $0.343(a/\lambda)$ and $0.378(a/\lambda)$ for both models, (a) for model-III, and (b) for model-IV. Insets are the super-cells for calculations.

It can be seen from Fig. 4 that for the two models, the multimode region supports more modes than the input waveguides at a given frequency within the band gap. This is due to the width difference between the input waveguides and the multimode regions. For later calculations and simulations, two operating frequencies of $0.343(a/\lambda)$ and $0.378(a/\lambda)$ are chosen as incident wave frequencies, corresponding to 1.66 THz and 1.83 THz, respectively. For the two models, the two frequencies ensure single-mode propagation in the input waveguides and multimode propagation in the multimode regions, as shown in Fig. 4 by the dashed lines.

3. Calculations and analyses of the PC MMI structures

In the two models shown in Fig. 3, the input waveguides are placed at the middle of left of the multimode regions. This forms a symmetric interference case [21]. From Fig. 4 it can be seen that for both models, there are 2 even modes at most in the multimode regions. This means that only two-fold images can be reproduced as folded images and a predicted image field distribution can be shown as Fig. 5.

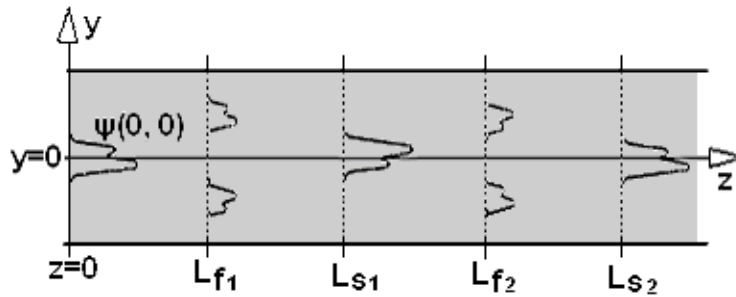


Fig. 5. Scheme of the image field distribution in the multimode region. A single image is at L_s and two-fold images are at L_f .

It should be pointed out that the self-imaging phenomena in the PC MMI structures are different from those in conventional waveguides [22]. This is due to the difference in guiding mechanisms. In the PC waveguides, wave guiding depends on photonic band gap confinement, while in conventional dielectric waveguides it depends on total internal reflection. This leads to an incapability of some approximations, such as weakly guiding.

In the multimode regions, all the guided modes are excited by the input field. Assuming that the input THz wave is continuous and the spatial spectrum of the input field is narrow enough not to excite unguided modes, the total field $\psi(y, z)$ in the multimode region can be decomposed into the guided modes and expressed as:

$$\psi(y, z) = \sum_{n=0}^{p-1} c_n \varphi_n(y) e^{-j\beta_n z} \quad (1)$$

where c_n is the field excitation coefficient, $\varphi_n(y) e^{-j\beta_n z}$ is the modal field distribution with a propagation constant β_n , p is the number of modes, and the subscript n denotes the order of the mode ($n = 0, 1, 2, \dots, p-1$). For simplicity, the initial phase of the input field at $z = 0$ is assumed to be 0, and therefore the input field at $z = 0$ should be

$$\begin{aligned} \psi(0, 0) &= \sum_{n=0}^{p-1} c_n \varphi_n(0) \\ &= c_0 \varphi_0(0) + c_1 \varphi_1(0) + c_2 \varphi_2(0) + c_3 \varphi_3(0) + \dots \end{aligned} \quad (2)$$

The field profile at a distance L can be written as a superposition of all guided mode field:

$$\begin{aligned}
\psi(0, L) &= \sum_{n=0}^{p-1} c_n \varphi_n(0) e^{-j\beta_n L} \\
&= c_0 \varphi_0(0) e^{-j\beta_0 L} + c_1 \varphi_1(0) e^{-j\beta_1 L} \\
&\quad + c_2 \varphi_2(0) e^{-j\beta_2 L} + c_3 \varphi_3(0) e^{-j\beta_3 L} + \dots
\end{aligned} \tag{3}$$

A single image, either a direct image or a mirrored one, is reproduced when $\psi(0, L) = \pm\psi(0, 0)$. By comparing the phase factors between terms in Eq. (2) and Eq. (3), the condition for the single image at $z = L_s$ is expressed as

$$\beta_n L_s = k_n \pi \quad \text{with } k_n = \begin{cases} 1, 3, 5, 7, \dots & \text{for mirrored image} \\ 2, 4, 6, 8, \dots & \text{for direct image} \end{cases} \tag{4}$$

And so L_s can be written as

$$L_s = \frac{k_n \pi}{\beta_n} \quad \text{with } k_n = \begin{cases} 1, 3, 5, 7, \dots & \text{for mirrored image} \\ 2, 4, 6, 8, \dots & \text{for direct image} \end{cases} \tag{5}$$

Apparently, L_s is periodical and has a constant interval of L_{s1} , where L_{s1} is at which the first single image is reproduced. It can be obtained by plugging the nearest positive integer sets $\{k_n\}$ into Eq. (5). So L_s can be rewritten as

$$L_s = k L_{s1} \quad \text{with } k = 1, 2, 3, \dots \tag{6}$$

The first two-fold images are symmetrically located along the y -axis, and can be obtained at $z = L_{f1}$ by linear combination of symmetric modes excited by the input field, where L_{f1} satisfies [21]

$$L_{f1} = \frac{L_{s1}}{2} \tag{7}$$

As all the other two-fold images can also be considered as linear combinations of symmetric modes excited by single image fields, the two-fold images can be found at $z = L_f$, where L_f satisfies

$$L_f = \left(k - \frac{1}{2}\right) L_{s1} \quad \text{with } k = 1, 2, 3, \dots \tag{8}$$

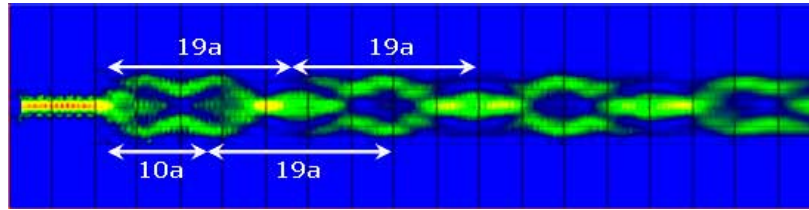
Therefore, the two-fold image distribution is also periodical and with the same interval as the single images. By using equations (5-8), imaging positions can be described. Tables 1 and 2 are the calculated imaging positions at the given operating frequencies for model-III and model-IV, respectively. In Tables 1 and 2, the initial value is defined as the distance between the start of the multimode region and the location where the first single image or two-fold image is reproduced, i.e., L_{s1} or L_{f1} .

Table 1. Results of calculated initial values and the intervals of L_s and L_f at a given operating frequency for model-III

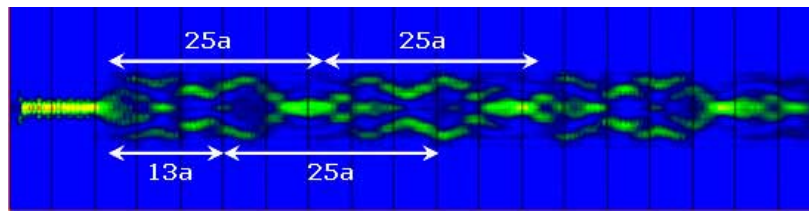
	0.343(a/λ) (1.66 THz)		0.378(a/λ) (1.83 THz)	
	initial value	interval	initial value	interval
L_s	19 a	19 a	25 a	25 a
L_f	10 a	19 a	13 a	25 a

Table 2. Results of calculated initial values and the intervals of L_s and L_f at a given operating frequency for model-IV

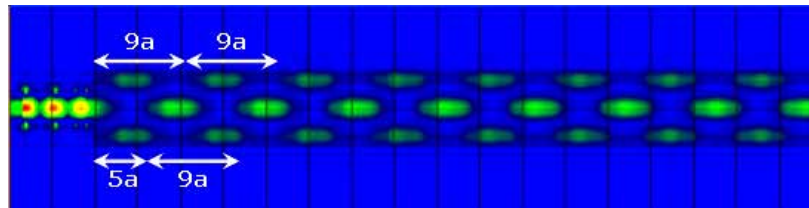
	0.343(a/λ) (1.66 THz)		0.378(a/λ) (1.83 THz)	
	initial value	interval	initial value	interval
L_s	$9a$	$9a$	$11a$	$11a$
L_f	$5a$	$9a$	$6a$	$11a$



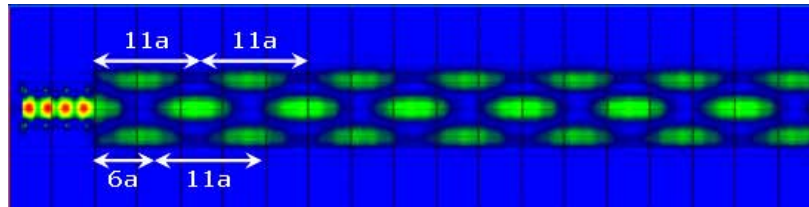
(a)



(b)



(c)



(d)

Fig. 6. FDTD simulated results of steady-state electric field distributions in the multimode regions for the continuous THz waves in model-III at (a) 1.66 THz, (b) 1.83 THz, and in model-IV at (c) 1.66 THz, (d) 1.83 THz.

4. Simulations and discussions

To demonstrate the MMI effects and self-imaging phenomena of the THz waves in the multimode regions, a numerical simulation is performed with the finite-difference time-domain (FDTD) method. As for model-III, to show the periodicity of the images, at least 3 single images or two-fold images are needed for both 1.66 THz and 1.83 THz. To take a

comparison, the length of multimode region in model-IV is set to be the same with that in model-III. Therefore the length of multimode region in simulations for both models is set to be $77a = 4774 \mu\text{m}$. By transforming the structures of Fig. 3 into the FDTD computational domain and launching THz waves at operating frequencies with corresponding polarizations, steady-state electric field distributions can be simulated and obtained, as shown in Fig. 6. It can be seen clearly that a single image and two-fold images are reproduced alternatively in constant intervals along the propagation direction in the multimode regions.

In Fig. 6, distances between the input fields and the first image fields are labeled with white lines, as well as the intervals between two adjacent images. These distances are got from the corresponding lengths listed in Tables 1 and 2. This provides a good agreement with the results derived from self-imaging principles in Section 3, and implies that MMI devices based on the self-imaging principle can be applied to THz wave region.

5. Design of THz wave filter and splitter based on the self-imaging principle

In this section, a THz wave filter and a splitter are demonstrated as an example of application of the previous work. The structures of the two devices are based on the models shown in Fig. 3(a) and 3(b), respectively. Output waveguides are connected on the right side of the MMI region by adding air holes or Si pillars. The device structures are shown in Fig. 7. The lengths of the multimode regions are calculated based on Eq. (6) and Eq. (8). As for the filter, the output waveguide is added at the position where a single image is reproduced for 1.66 THz and a two-fold image is reproduced for 1.83 THz. Therefore, $L_s = 2L_{s1} = 2 \times 19a = 38a$ is calculated at $k = 2$ for 1.66 THz and $L_f = (2 - 1/2)a = 1.5 \times 25a \approx 38a$ is calculated for 1.83 THz. As a result, a length of $38a$ is chosen for the filter. For the splitter, the length of the multimode region should ensure reproducing a two-fold image for both 1.66 THz and 1.83 THz. By analogy, the sixth ($k = 6$) and the fifth ($k = 5$) two-fold images can be obtained at $L_f \approx 58a$ for 1.66 THz and 1.83 THz, respectively. So, a length of $58a$ is chosen for the splitter. To excite the waveguides in practical applications, a THz time-domain spectroscopy (TDS) can be used, with two Plano-cylindrical silicon lenses placed at the confocal beam waist of the THz-TDS to couple the THz wave signals into and out of the waveguides, as applied in reference [19].

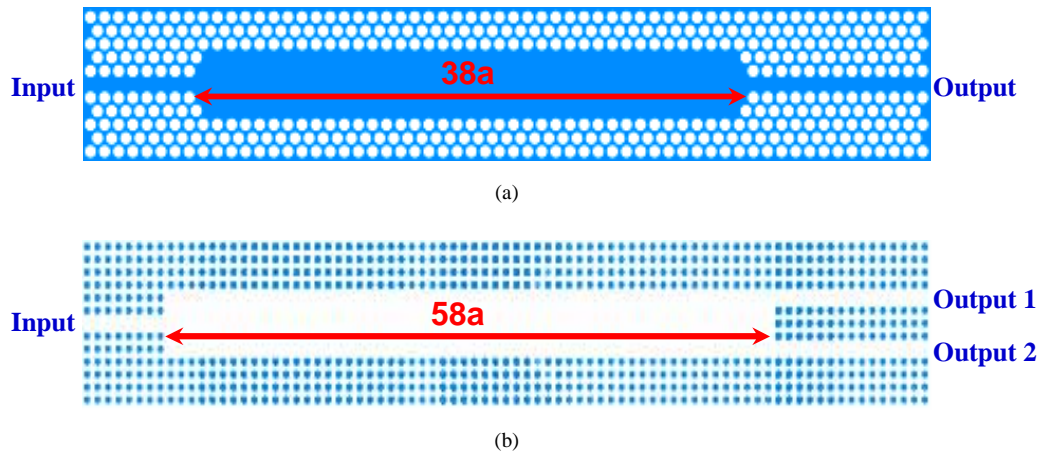
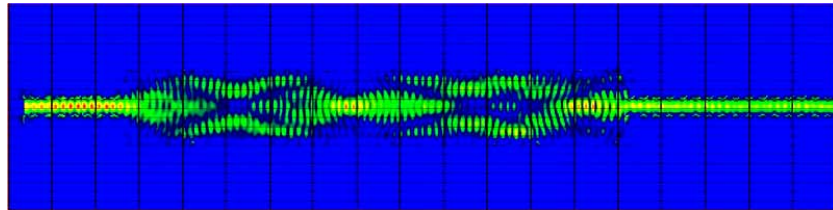


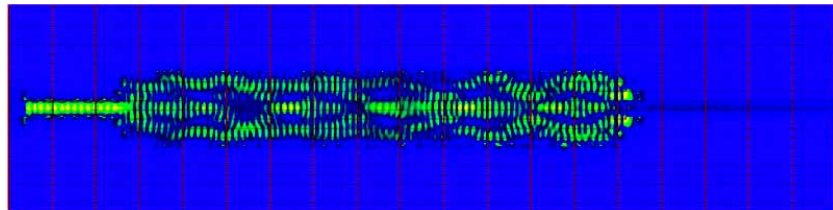
Fig. 7. Schematic diagrams for the ichnography of the Si PC waveguide-based devices: (a) THz wave filter, (b) THz wave splitter. Thickness of the filter and the splitter is $37 \mu\text{m}$ and $100 \mu\text{m}$, respectively. Total length of the filter and splitter is $3534 \mu\text{m}$ and $4898 \mu\text{m}$, respectively. Width of the filter and the splitter is $640 \mu\text{m}$ and $828 \mu\text{m}$, respectively.

The performances of the two devices are also demonstrated with simulations by the FDTD method and the field profiles are shown in Fig. 8. The power transmittances are figured out by setting up observation lines centered at the output waveguides for both devices.

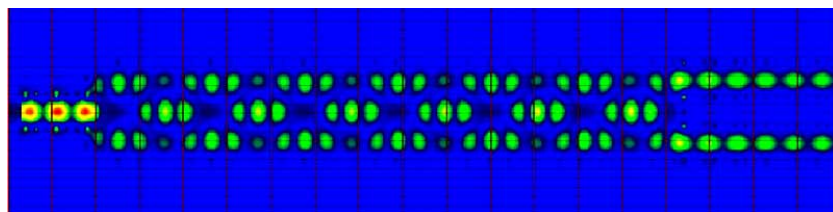
From the Fig. 8, it can be seen that the 1.66 THz wave can be output from the output waveguide of the proposed THz wave filter, with a calculated power transmittance of 98% (Fig. 8(a)), while the 1.83 THz wave is totally reflected back with a reflection power of 95% (Fig. 8(b)). This means the device can filter 1.66 THz wave from those combined with 1.83 THz. Further more it can be seen from the Figs. 8(c) and 8(d) that both the 1.66 THz and the 1.83 THz waves are divided into two parts and output from the two parallel output waveguides. The calculated losses are 0.2 dB and 0.17 dB for Figs. 8(c) and 8(d), respectively.



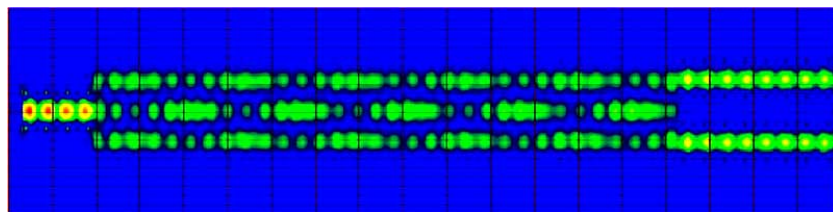
(a)



(b)



(c)



(d)

Fig. 8. FDTD simulated electric field profiles in the two designed devices. (a) 1.66 THz wave field profile in the filter, (b) 1.83 THz wave field profile in the filter, (c) 1.66 THz wave field profile in the splitter, and (d) 1.83 THz wave field profile in the splitter.

6. Summary

The applicability of MMI effect and self-imaging principle for THz waves in 2D Si photonic crystal waveguides is investigated with modeling, calculating and simulating. The results show that the MMI effect and the self-imaging principle are applicable for THz waves. As an example, a THz waveguide filter and a splitter are proposed and their performances are demonstrated at frequencies of 1.66 THz and 1.83 THz which are informative for absorption in majority large biomolecules. Besides, as Si shows a transparency for THz waves below 10 THz, it would be a kind of promising material to propagate THz waves. Accordingly, Si PC waveguides would be preference devices to guide THz waves. It is also expected that applications of Si PC waveguide devices based on MMI effects can be found in THz medical imaging, chemical testing and biological sensing.

Acknowledgments

This work was supported in part by the National Natural Science Foundation of China (Nos. 90401008, 60577001), the Key Project of Chinese Ministry of Education (No. 104144), the Research Fund for the Doctoral Program of Higher Education (No. 20040558009), and the Program for New Century Excellent Talents in University (No. NECT-04-0796).